Contents lists available at ScienceDirect

Nuclear Inst. and Methods in Physics Research, A

Unveiling short-range magnetic correlations: The development of magnetic pair distribution function method at CSNS

Long Yang [a,*], Te Kang [a], Juping Xu [b,c,**], Wen Yin [b,c]

[a] *Interdisciplinary Materials Research Center, School of Materials Science and Engineering, Tongji University, 4800 Caoan Road, Shanghai, 201804, China*
[b] *Institute of High Energy Physics, Chinese Academy of Sciences (CAS), Beijing, 100049, China*
[c] *Spallation Neutron Source Science Center (SNSSC), Dongguan, 523803, China*

A B S T R A C T

Recent advancements in the magnetic pair distribution function (mPDF) analysis of neutron total scattering data provide a powerful approach to investigate local magnetic correlations in materials. This technique is promising for revealing short-range magnetic correlations at the sub-nanometer length scale directly in real space. It is particularly suitable for strongly correlated electron systems and geometrically frustrated magnets. In this study, the mPDF experiment is conducted at the multi-physics instrument (MPI) of the China Spallation Neutron Source, one of the latest neutron total scattering diffractometers in the world. We systematically benchmarked a series of important parameters related to the experimental setup and data processing for mPDF experiments at the MPI and similar instruments. This method not only advances the magnetic structure determination of fundamental materials but also opens the door for extending mPDF studies to more complicated and frontier magnetic systems that are challenging for conventional diffraction methods.

1. Introduction

Exotic magnetic properties in advanced materials have aroused significant interest over the decades, including high-temperature superconductivity [1,2], colossal magnetoresistance [3–5], and multiferroics [6,7]. To further investigate the physical mechanisms behind these phenomena, it is essential to characterize the precise magnetic structures of materials.

Since the 1950s, neutron diffraction has been established as one of the most powerful probes for investigating the magnetic structures and properties of materials. Neutrons possess intrinsic magnetic moments for detecting the spins in materials, and thermal neutrons with the energy scale of tens to hundreds of meV could have appropriate wavelengths on the order of Ångströms, which are comparable to atomic arrangements in condensed matter. For instance, neutron diffraction successfully solved the magnetic structure of MnO, one of the most important antiferromagnetic structures in the history [8,9]. Nevertheless, conventional neutron diffraction is usually applied for determining the long-range ordered magnetic structures, which mainly analyzes the magnetic Bragg peaks from the diffraction pattern [8,10]. This technique is sensitive to the long-range average structure of a material, and is therefore poorly suited to the study of short-range local structure in exotic materials.

At the frontiers of condensed matter research, the local short-range magnetic ordering is key to understanding their unique and exciting physical properties, such as spin fluctuations in quantum spin liquids [11,12], disordered states in spin glasses [13,14], and spin orders in diluted magnetic semiconductors [15,16].

The total scattering technique has been proven to be an effective tool for investigating local atomic structures over the past two decades [17–20]. Total scattering considers both Bragg peaks and diffuse scattering signals, which refer to the long-range structural ordering and short-range correlations, respectively. Atomic pair distribution function (PDF) analysis of total scattering data can reveal the local atomic structures of complex materials directly in real space [17]. PDF analysis involves Fourier transforming the scattered intensity from scattering momentum Q space into real space, requiring a relatively high Q range to obtain high real-space resolution in the atomic PDF analysis.

The magnetic pair distribution function (mPDF) technique, utilizing a neutron total scattering experiment [21], has been recently developed to investigate the local short-range magnetic correlations [22–24]. Successful mPDF experiments were demonstrated at spallation neutron sources utilizing the NPDF instrument at the Los Alamos Neutron Science Center (LANSCE) [25] and the NOMAD instrument at the Spallation Neutron Source (SNS) [26], and more recently, the HYSPEC instrument at the SNS [23] and the NOVA instrument at the Japan

---

* Corresponding author.
** Corresponding author. Institute of High Energy Physics, Chinese Academy of Sciences (CAS), Beijing, 100049, China.
E-mail addresses: long_yang@tongji.edu.cn (L. Yang), xujuping@ihep.ac.cn (J. Xu).

Proton Accelerator Research Complex (J-PARC) [27]. In addition, since the required Q range for mPDF is usually less stringent than for atomic PDF, some mPDF experiments have also been attempted at the diffraction instruments of reactor-based neutron sources, such as the D4 of the Institut Laue-Langevin (ILL) [28] and the HB-2A at High Flux Isotope Reactor (HFIR) [29].

The multi-physics instrument (MPI) at China Spallation Neutron Source (CSNS) is the latest built total scattering neutron time-of-flight (TOF) diffractometer in China, and it features high flux and high Q range for conducting a PDF experiment [30]. In this work, we carried out the first mPDF experiment at the MPI instrument. The antiferromagnetic MnO and altermagnetic MnTe polycrystalline powders were used as example samples to benchmark the experimental setup, data processing, and local magnetic structural modeling procedures at the MPI. The MnO system, a classic antiferromagnetic material, has been studied by neutron diffraction since the mid 1950s [8,31]. The mPDF methodology was first demonstrated in MnO, effectively revealing that MnO has a locally monoclinic structure but tends toward the average rhombohedral $R\bar{3}m$ symmetry. For the paramagnetic phase above the Néel temperature $T_N \approx 118$ K, mPDF analysis unveiled significant short-range magnetic correlations [32]. Due to its strong mPDF signals, MnO has been used across different instruments for benchmarking mPDF analysis, including the NPDF instrument at LANSCE, NOMAD instrument at SNS, and D20 instrument at the Institute Laue-Langevin (ILL) [22,33]. Additionally, MnTe (atomic structure space group: $P6_3/mmc$) has an altermagnetic order of ferromagnetic ab planes, stacked antiferromagnetically along the c axis [34]. Despite the simple antiferromagnetic configuration, it exhibits significant short-range magnetic correlations above the Néel temperature, which seem to enhance the thermoelectric performance [35–37]. The local antiferromagnet-like fluctuations (paramagnons) may be potentially characterized by a mPDF experiment at the MPI.

Parameters related to the neutron total scattering experiment, such as measurement time, Q range, and data smoothing modifications, were also studied systemically. These parameter choices may serve as a benchmark for researchers interested in conducting mPDF experiments to reveal magnetic correlations directly in real space, whether at the MPI or other similar instruments. Furthermore, this study opens up possibilities for developing additional mPDF-related methodologies at the facility in the future, such as utilizing polarized neutron instruments to separate magnetic signals and employing single crystal neutron diffraction for three-dimensional mPDF [23,38].

2. Methods and data processing

2.1. The multi-physics instrument

The MPI utilizes beam port #16 of the CSNS target station, facing the center of a decoupled water moderator. The MPI standard operating wavelength range is 0.1–4.5 Å with a peak flux at around 1.2 Å. The neutron flux at the sample position was about 4.23×10^7 n/cm^2/s with the accelerator operated at a power of 140 kW. The detector of MPI is consisted of ^{3}He tubes, which are divided into 7 banks, where bank #1 is under the construction. The detectors cover a scattering angle 2θ range currently from 12.54° to 170.00°, corresponding to a Q range of 0.3–125 Å^{-1} as simulated by Bragg's Law, ensuring coverage of a sufficiently high Q range while maintaining appropriate Q space resolution. A detailed introduction of MPI can be found in Xu et al. [30]. Since magnetic scattering usually occurs at low Q, the Q_{min} was set as 0.5 Å^{-1} to best retain the low-Q magnetic scattering signals for the materials under study in this work, and balancing the low signal-to-noise ratio at the edge of the wave band. Typically, the MPI instrument can get sufficient neutron counts within the Q range below 40 Å^{-1}, and PDF data processed with different Q_{max} values ranging from 10.0 Å^{-1} to 31.5 Å^{-1}

have been tested, which will be discussed later. The low-temperature sample environment CCR06 was utilized during the experiment, providing a sample environment temperature range of 5 K–600 K.

2.2. Material synthesis

Polycrystalline MnO (99.99%) powders with mass 2.90 g were purchased from a commercial vendor (aladdin-e.com). Polycrystalline MnTe samples (4.94 g) were synthesized by melting stoichiometric amounts of elemental Mn (99.8%) and Te (99.99%) in the graphite-coated and vacuum-sealed quartz tubes at 1273 K for 6 h, quenching in cold water, and annealing at 923 K for 72 h, following the literature [39]. Both samples were hand ground into fine powders through a 300-mesh sieve for neutron scattering experiments. The powders were loaded into a 9-mm inner-diameter Vanadium can at the MPI. After sample loading, the height of both samples is kept the same as 28 mm. The Vanadium can was sealed by metal Indium rings in an argon glovebox.

2.3. MPDF data processing and structural modeling

After the collection of raw diffraction patterns, both atomic PDF and mPDF data are processed in the same procedures, as illustrated in Fig. 1. We first stitch diffraction patterns from different banks to obtain the structure function $S(Q)$. We retain the low angle data and bring up to large Q by the high angle. The data ranges of each bank in the stitching are listed in Table S1; next, data corrections such as normalization, absorption correction, and incoherent signal removal, are performed using the Mantid software [40]; subsequently, the data are Fourier transformed from reciprocal space to real space, and experimental PDFs are obtained finally. The diffraction patterns are represented in units of d-spacing in Fig. 1(a) and (d), for MnO at 20 K and 300 K, respectively. The processed structure function $S(Q)$ and PDF $G(r)$ are shown in the middle and right columns of Fig. 1, respectively. In addition, we have also tested the Lorch function as the Fourier filter in the Fourier transform to validate how it would affect the mPDF data quality at the MPI [41].

For polycrystalline powder samples, both atomic (nuclear) and magnetic scattering signals are collected together in an unpolarized neutron scattering experiment. The local atomic structure was studied using the atomic pair distribution function (PDF) technique, which provides the interatomic distance distribution, i.e., the probability of finding atomic pairs of distance r apart [17,20]. The experimental atomic PDF, denoted $G_{nuc}(r)$, is the truncated Fourier transform of the total scattering structure function.

$$G_{nuc}(r) = \frac{2}{\pi} \int_{Q_{min}}^{Q_{max}} Q[S(Q)-1]sin(Qr)dQ \qquad (1)$$

where Q is the magnitude of the scattering momentum transfer. The total scattering structure function, $S(Q)$, is extracted from the Bragg and diffuse components of neutron powder diffraction intensity.

The atomic PDF modeling program DiffPy-CMI is used for local atomic structure refinements against experimental PDF [42]. For a given atomic structure, the atomic PDF can be calculated according to

$$G_{nuc}(r) = 4\pi r[\rho_a(r) - \rho_{a0}], \qquad (2)$$

$$\rho_a(r) = \frac{1}{4\pi r^2 N_a} \sum_i \sum_{i \neq j} \frac{b_i b_j}{\langle b \rangle^2} \delta(r - r_{ij}). \qquad (3)$$

Here, ρ_{a0} is the atomic number density of the material, and $\rho_a(r)$ is the atomic pair density, which is the mean weighted density of neighbor atoms at a distance r from an atom at the origin. The sums in $\rho_a(r)$ run over all atoms in the sample, where N_a is the number of atoms in the system, b_i is the coherent neutron scattering length of atom i, $\langle b \rangle$ is the
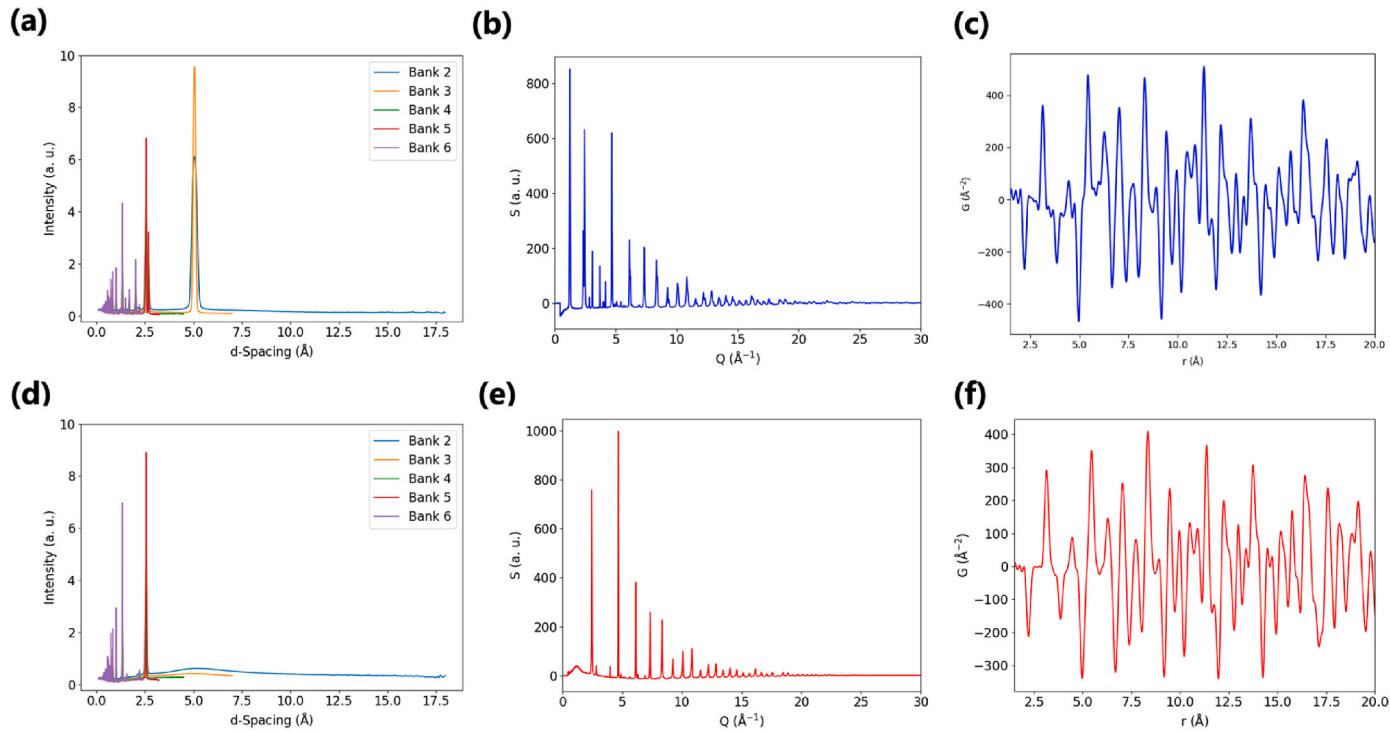
Fig. 1. The PDF data processing of MnO measured at the MPI. (a) and (d): The diffraction patterns at (a) 20 K and (d) 300 K in units of d-spacing (Å). (b) and (e): The structure functions at (b) 20 K and (e) 300 K after stitching banks. (c) and (f): The experimental PDFs at (c) 20 K and (f) 300 K using $Q_{max} = 25.0$ Å^{-1}.

average coherent neutron scattering length in the system, and r_{ij} is the distance between atoms i and j.

The mPDF is analogous to the atomic PDF expression, but is in terms of the magnetic form factor $f_{mag}(Q)$ instead of the neutron scattering length b. For an isotropic polycrystalline sample of a typical magnetic material possessing localized spins that belong to a single magnetic species, the mPDF is given by [21]

$$G_{mag}(r) = \frac{2}{\pi} \int_{Q_{min}}^{Q_{max}} Q \left[\frac{(d\sigma/d\Omega)_{mag}}{\frac{2}{3} N_s S(S+1)(\gamma r_0)^2 f_{mag}^2(Q)} - 1 \right] sin(Qr) dQ \qquad (4)$$

$$= \frac{3}{2S(S+1)} \left(\frac{1}{N_s} \sum_{i \neq j} \left[\frac{A_{ij}}{r} \delta(r - r_{ij}) + B_{ij} \frac{r}{r_{ij}^3} \Theta(r_{ij} - r) \right] - 4\pi r \rho_{s0} \frac{2}{3} m^2 \right), \qquad (5)$$

where $(d\sigma/d\Omega)_{mag}$ is the magnetic differential scattering cross section [43], the subscripts i and j refer to individual magnetic moments $\boldsymbol{S}_i$ and $\boldsymbol{S}_j$ separated by a distance r_{ij}, $A_{ij} = \langle S_i^y S_j^y \rangle$, $B_{ij} = 2\langle S_i^x S_j^x \rangle - \langle S_i^y S_j^y \rangle$, S is the spin quantum number in units of $\hbar$, $r_0 = (\mu_0/4\pi)(e^2/m_e)$ is the classical electron radius, $\gamma = 1.913$ is the neutron magnetic moment in units of nuclear magnetons, N_s is the number of spins in the system, Θ denotes the Heaviside step function, ρ_{s0} is the number of spins per unit volume, and m is the average magnetic moment in μ_B, which equals zero if no net magnetization, such as antiferromagnets. Eqn. (4) defines the experimental mPDF, while Eqn. (5) shows how to simulate the mPDF for a given magnetic structure.

The experimentally collected diffraction datasets treat magnetic scattering the same as nuclear scattering in the PDF data processing protocol, and does not include normalizing the magnetic scattering by the squared magnetic form factor. This has the effect of broadening the $G_{mag}(r)$ by approximately $\sqrt{2}$ times the real-space extent of the electronic wavefunction giving rise to the magnetic moment. This non-deconvoluted mPDF (also called unnormalized mPDF) takes the form of

$$d_{mag}(r) = \frac{2}{\pi} \int_{Q_{min}}^{Q_{max}} Q \left(\frac{d\sigma}{d\Omega} \right)_{mag} sin(Qr) dQ \qquad (6)$$

$$= C_1 \times G_{mag}(r) * S(r) + C_2 \times \frac{dS}{dr}, \qquad (7)$$

where C_1 and C_2 are constants related by $C_1/C_2 = -1/\sqrt{2\pi}$ in the fully ordered state, * represents the convolution operation, and $S(r) = \mathscr{F}\{f_{mag}(Q)\} * \mathscr{F}\{f_{mag}(Q)\}$ (where $\mathscr{F}$ denotes the Fourier transform). The quantity $\mathscr{F}\{f_{mag}(Q)\}$ is closely related to the real-space magnetic moment density.

Therefore, the experimental neutron total PDF signals can be separated into nuclear and magnetic contributions

$$G_{tot}(r) = G_{nuc}(r) + d_{mag}(r) / (N_a \langle b \rangle^2). \qquad (8)$$

The local structural refinement is performed by the diffpy.mpdf program within the DiffPy-CMI software framework [33,42]. For the atomic structural modeling, the following parameters are applied. The lattice parameters of MnO and MnTe are constrained according to the reported crystal systems [44,45]. The anisotropic atomic displacement parameters (ADPs), U_{11} (Å^2) and U_{33} (Å^2), are applied based on the crystal symmetry. The ADPs of the same type of atoms are constrained to be the same. δ_1 (Å) is a parameter that describes correlated atomic motions [46].

Unlike the atomic PDF, the mPDF contains both spatial and orientational magnetic correlations. For mPDF structural refinements, a series of parameters are free to refine to obtain the best fit, including the paramagnetic scale factor (corresponding to the self-scattering component of the magnetic differential scattering cross section), the ordered scale factor (related to the square of the locally ordered magnetic moment), and the direction of the magnetic moments can be described by the θ and ϕ angles, as defined by the angles from the c and a crystallographic axes, respectively, i.e., $[\sin\theta\cos\phi, \sin\theta\sin\phi, \cos\theta]$. Notice

that the ϕ angle value does not make any difference to the mPDF of MnO and MnTe, due to their structural symmetries, so ϕ is fixed as 0 during the fit. *MSPD* (Å) is a parameter that accounts for the correlation length, or more precisely, the domain size of coherent magnetic scattering in the material.

Here we use the damped least-squares method (Levenberg–Marquardt algorithm) [47,48], which is deployed in the Python programming package SciPy [49], to vary the adjustable parameters to achieve the best agreement between the calculated and measured PDFs. The fit quality is described by the goodness-of-fit R_w, given by

$$R_w = \left\{ \frac{\sum_{i=1}^{n} [G_{\text{obs}}(r_i) - G_{\text{calc}}(r_i, P)]^2}{\sum_{i=1}^{n} G_{\text{obs}}(r_i)^2} \right\}^{1/2}, \tag{9}$$

where G_{obs} and G_{calc} are the observed and calculated PDFs, respectively, and P is the set of parameters refined in the model.

The conventional Rietveld refinements for confirming the long-range average atomic structure are carried out using the GSAS-II software [50]. The MnO and MnTe magnetic structures used during the mPDF modeling are obtained from the MAGNDATA structure database [44,45, 51].

3. Results and discussions

3.1. Atomic structural modeling

Before looking into real space, we first investigate the reciprocal space neutron diffraction data collected at the MPI. The low-angle bank #2 diffraction patterns of the MnO sample at 20 K and 300 K are plotted in Fig. 2(a). The magnetic Bragg peak at $Q = 1.24 \text{ Å}^{-1}$ is very sharp at the low-temperature antiferromagnetic phase. At high temperature (300 K), the sharp magnetic Bragg peak merges into broad and weak

diffuse scattering signals, which are usually omitted in conventional neutron diffraction analysis, but are prominent in mPDF local magnetic structural modeling. The Rietveld refinements for the MnO atomic structure are shown in Fig. 2(b) and (c) for low and high temperature data, respectively. As expected, the magnetic Bragg peak arising at 20 K cannot be described by atomic scattering contributions.

Now let us move to the real-space PDF data. In a neutron total scattering experiment, both atomic and magnetic scattering signals are collected altogether, resulting in neutron PDF data containing both contributions. As shown in Fig. 2(d), the experimental total PDFs of MnO at 20 K and 300 K are plotted together, and all the PDF peak positions are aligned reasonably well, indicating that the crystal structure does not change much, and the rock-salt cubic average structure (space group: $Fm\bar{3}m$) in the high-temperature paramagnetic phase distorts slightly to a rhombohedral structure (s.g.: $R\bar{3}m$) while cooling to the low-temperature magnetically ordered phase. In addition, the measured PDF data at low temperature have different amplitudes at all the peak positions, since the mPDF signals of magnetically ordered phase are added to the atomic ones when below the Néel temperature (the total PDF peaks have larger amplitudes if the mPDF has positive values, and smaller amplitudes if negative).

Quantitative atomic PDF refinements were performed for both low and room temperature MnO data, with the fit results shown in Fig. 2(e) and (f), respectively. At low temperature (20 K), after subtracting the atomic PDF contribution from the experimental neutron total PDF, the remaining magnetic signals are prominent, represented by green curves offset below, indicating significant antiferromagnetic correlations in MnO. In contrast, the experimental PDF at 300 K primarily exhibits atomic PDF signals, as indicated by the small difference curve in Fig. 2 (f).

3.2. Fourier tansform Q_{max}

In the mPDF local structural refinement, an initial atomic and
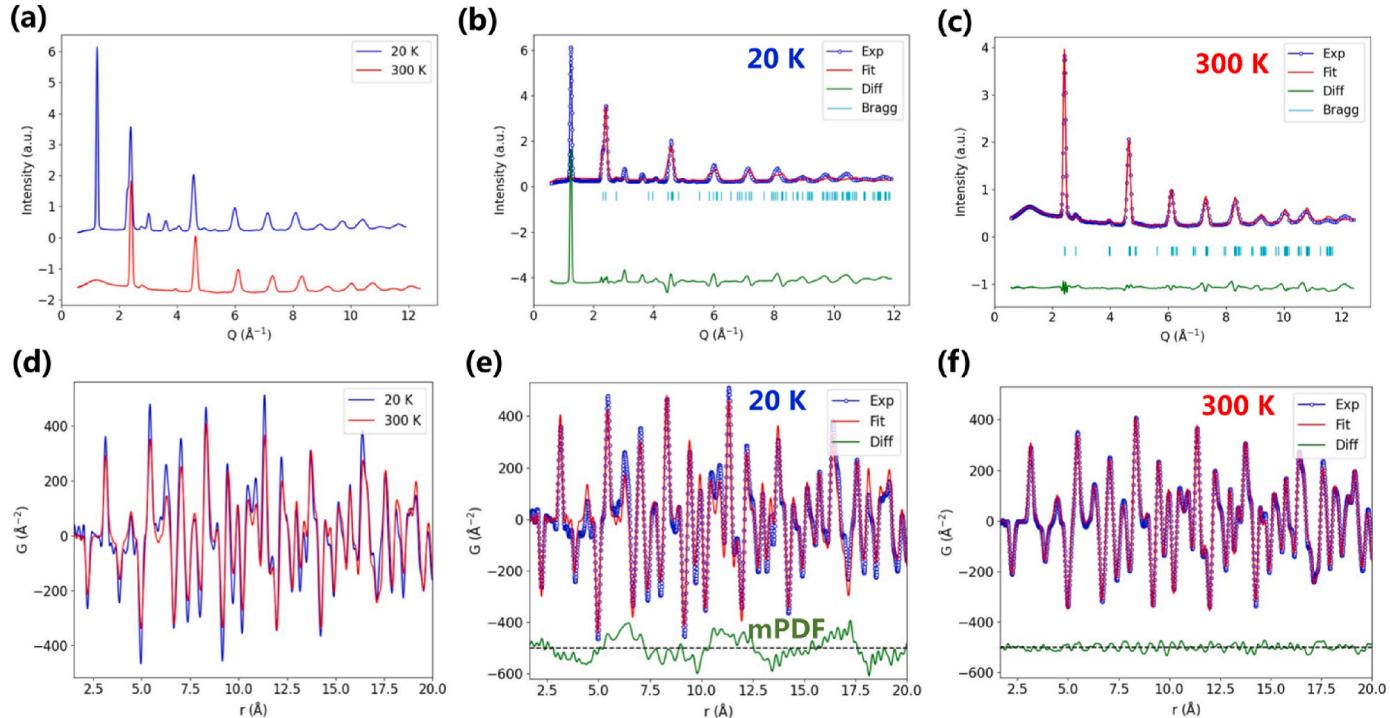

Fig. 2. (a) The experimental diffraction patterns of MnO at 20 K (blue curve) and 300 K (red curve). (b) and (c): The experimental diffraction data (blue circles) at (b) 20 K and (c) 300 K are fit by the MnO atomic structure (red curves), and the difference curves (light blue) are shown offset below. (d) The experimental PDFs of MnO at 20 K (blue curve) and 300 K (red curve) using $Q_{max} = 25.0 \text{ Å}^{-1}$. (e) and (f): The experimental PDF data (blue circles) at (e) 20 K and (f) 300 K are fit by the MnO atomic structure (red curves) over the range of $1.5 < r < 20.0$ Å, and the difference curves (green) are shown offset below.

magnetic structure model needs to be built first. For MnO, the rhombohedral structure is applied for the atomic PDF model at all temperatures. Below the Néel temperature (118 K), the magnetic transition is accompanied by a rhombohedral compression of the lattice along the [111] direction (the rhombohedral lattice is derived from the cubic one). The spins of the Mn^{2+} ions lying within common (111) planes align ferromagnetically, with antiferromagnetic alignment between adjacent planes along the [111] direction, forming a type-II antiferromagnetic structure, as shown in Fig. 3(a) [31,44].

Analogous to atomic PDF technique, different Q_{max} choices determine the real-space resolution of the short-range magnetic structure in mPDF. Data processed with Q_{max} ranging from $10.0\,\text{Å}^{-1}$ to $31.5\,\text{Å}^{-1}$ are tested systematically to characterize the mPDF data quality at the MPI.

The PDF data using different Q_{max} are shown in Fig. S1. The PDF peak positions are distinguishable, such as the nearest neighbor Mn–O bond, represented by the negative peak at $r = 2.2\,\text{Å}$, and the second nearest neighbor atom pair, i.e., the positive peak at $r = 3.1\,\text{Å}$. However, the real-space resolution may be too low if a small Q_{max} Fourier transform cutoff is applied, resulting in PDF peaks that are too broad to distinguish individual atom pairs.

The atomic and magnetic PDF structural refinement results are compared using different Q_{max}, as shown in Fig. 3. The blue circles represent the experimental PDF collected at the MPI, with the best-fit total PDF overlaid in red. The isolated mPDF component is given by the gray curve offset below, with the best-fit unnormalized mPDF shown by the blue curve. The overall fit (atomic plus magnetic PDF) residual is displayed in the green curve near the bottom. The PDF fit qualities are similar, as described by the goodness-of-fit R_w parameter in Fig. S2. The detailed structural refinement results are listed in Table S2. The PDF processed with $Q_{max} = 25.0\,\text{Å}^{-1}$ gives the best fit quality (the lowest goodness-of-fit parameter R_w). If the Q_{max} is set too low (such as $Q_{max} = 10.0\,\text{Å}^{-1}$), the PDF peaks become significantly broadened,

which is not sufficient for obtaining high-resolution real-space information. Even though considering that magnetic form factors decay quickly with scattering momentum Q, the real-space resolution of the magnetic structure may not be greatly affected by using a low Q_{max}. In some cases, if the atomic structure has been previously resolved, collecting neutron total scattering data using a beamline with limited Q range could also be acceptable for the mPDF study [23,29]. Since atomic and magnetic structures are highly related with each other (determining the location of spins requires the atomic site information), it is best to resolve both parts with high real-space resolution. In the following, we will use the $Q_{max} = 25.0\,\text{Å}^{-1}$ datasets as representative results for discussions.

3.3. Refinement heuristics

Since neutron powder diffraction data contain both nuclear and magnetic scattering signals, we need to separate them during the structural refinement. To address this challenge, two refinement strategies were tested for modeling the local structure in real space: 1) Toggle mode: in one cycle, it first performs the atomic PDF structural refinement against the experimental PDF data, and then all the atomic structural parameters are fixed, followed by the mPDF refinement against the residual. This can be repeated (by three times in this work) to obtain further optimized results. 2) Co-refinement mode: it calculates both atomic and magnetic PDF signals, sums them up to fit against the experimental PDF, and refines both the atomic and magnetic structures simultaneously.

For the MnO data at 20 K, both refinement modes yield nearly identical fit quality, as demonstrated in Fig. S3. They effectively resolved the atomic structure and antiferromagnetic alignment along the [111] direction in real space (see insets of Fig. S3). The refined magnetic structure closely matches the literature reported results obtained from the NPDF instrument [22] and the NOMAD instrument [33].
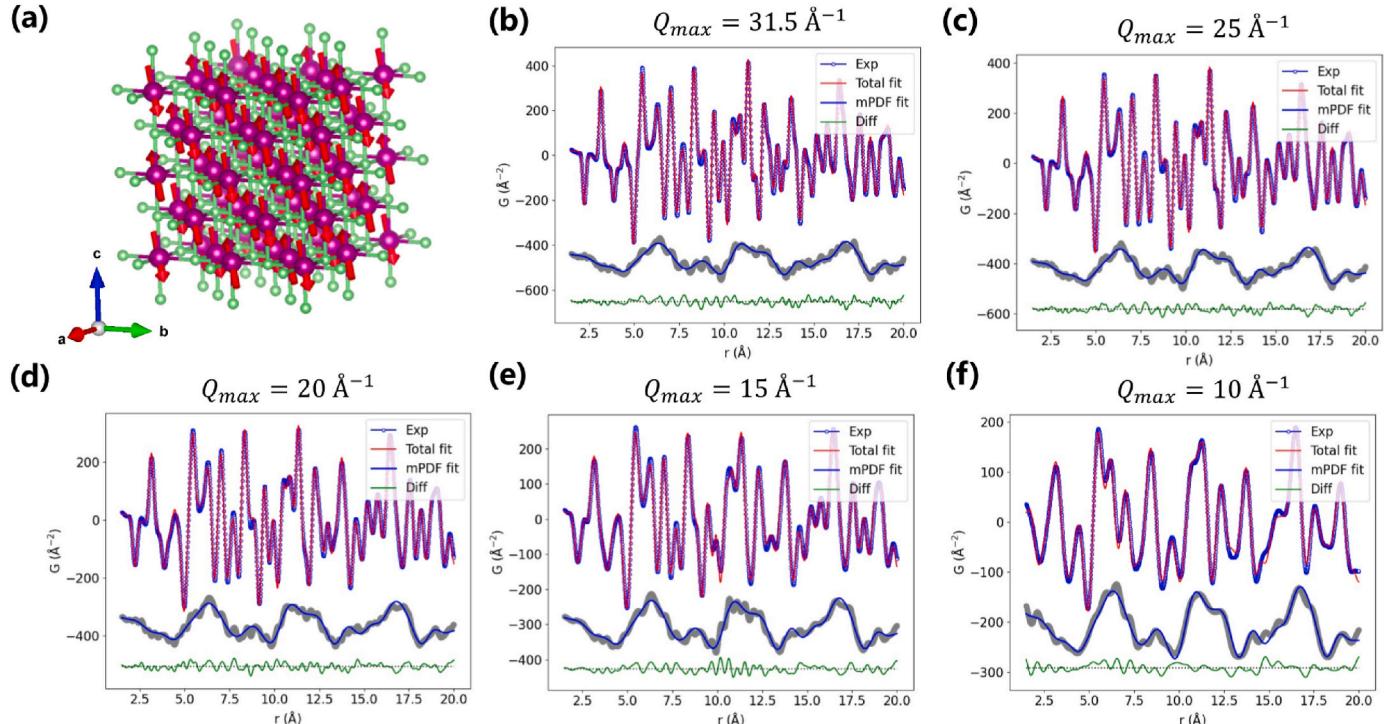

Fig. 3. (a): The atomic and magnetic structure of MnO, where Mn and O atoms are shown in purple and green, respectively, and the magnetic moments on Mn sites are represented by red vectors. (b–f): The combined atomic and magnetic PDF structural refinements for MnO at 20 K. The experimental total PDF datasets with different Q_{max} are plotted in blue circles, the calculated total PDF of the best-fit structure is shown in the red curve, the isolated mPDF experimental pattern and the mPDF fit are displayed in the gray and blue curves, respectively, offset just below, and the overall fit residual is shown in the green curve at the bottom.

Thus, MPI is capable of collecting high-quality mPDF data.

3.4. Data smoothing

We also investigated the impact of applying a modification function to the mPDF data collected at the MPI. The modified PDF is expressed as $G_{mod}(r) = 2/\pi \int_{Q_{min}}^{Q_{max}} Q[S(Q)-1]sin(Qr)M(Q)dQ$, where $M(Q)$ represents the modification function, typically the Lorch function for neutron data. We employed the conventional Lorch function, defined as $M_L(Q) = (Q_{max}/\pi Q)\sin(\pi Q/Q_{max})$ if $Q \leq Q_{max}$ and 0 elsewhere [41], as shown in Fig. S4(a) for $Q_{max} = 25.0\,\text{Å}^{-1}$.

For magnetic PDF fits, as shown by the solid blue curves offset below in Fig. S4(b) and (c) for raw and modified data, respectively, the application of the Lorch function does not quite affect the mPDF structural refinement results, as indicated by the similar mPDF fits. This is because the Lorch window with $Q_{max} = 25.0\,\text{Å}^{-1}$ has little impact on non-deconvoluted mPDF patterns, i.e., $d_{mag}(r)$ in Eqn. (6), with the fast dampening squared magnetic form factor of Mn^{2+}, which is primarily limited within low Q [23]. However, for atomic PDF fits, applying the Lorch function may help improve the structural refinements by suppressing the effects of statistical or systematic errors in the scattering data at high Q, thereby reducing high-frequency ripples in the PDF. Nevertheless, this improvement comes at the cost of reduced real-space resolution and the possible loss of physically meaningful information. Therefore, the application of Lorch functions has little impact on mPDF local magnetic structural modeling as long as a sufficiently large Q_{max} is achieved in the experiment.

3.5. Data acquisition

In addition, the mPDF method is applied to study the other magnetic system, the altermagnetic MnTe material, which has recently received attention in both basic research and energy application, including the fields of condensed matter physics and thermoelectrics [36,52]. In MnTe, the Mn^{2+} magnetic moments in MnTe form antiferromagnetic ordering below the Néel temperature ($T_N \approx 307$ K) with the hexagonal NiAs structure type [45,53]. Specifically, the spins align ferromagnetically within hexagonal *ab* planes and antiferromagnetically between planes along the crystallographic *c* axis [45]. The magnetic structure is visualized in Fig. S5. The paramagnon drag in MnTe represents a state where short-range magnetic correlations persist across the antiferromagnetic-paramagnetic phase transition, despite the absence of long-range magnetic order. A real-space direct observation of such short-range antiferromagnetic correlations by the mPDF method would enable a more comprehensive understanding of the underlying physical mechanism.

To benchmark the measurement time required for collecting satisfactory mPDF data, different data acquisition time was benchmarked for MnTe ranging from 2 to 8 h with a 2-h step, as shown in Fig. 4(a) for the data at 20 K. The mPDF refinement results (Fig. 4 and Table S3) are nearly identical for data collected from 2 h to 8 h. Owing to the high flux available at the MPI (which would be further increased in the future facility upgrade plan), high-quality mPDF data of this magnetic system can be obtained within as little as 2 h.

Interestingly, in the regime of long-range paramagnetic phase at high temperature (400 K), which is well above its Néel temperature, the mPDF fit shows a local antiferromagnetic state in MnTe, with a magnetic correlation length of less than 1 nm, indicated by the antiferromagnetic mPDF signals at low-*r* in Fig. 4(d). The detailed mPDF refinement results of MnTe data at 400 K can be found in Table S4. As revealed by mPDF analysis, the significant short-range magnetic correlations exist in the paramagnetic state above the Néel temperature, i.e., the paramagnons, which could change the transport properties of materials. For MnTe, the paramagnon drag effect enhances the thermopower, making it a promising thermoelectric material candidate [36,37]. Therefore, the mPDF method is suitable for obtaining the short-range magnetic ordering information at the sub-nanometer length scale, which is often veiled in the long-range average structure from a conventional neutron diffraction experiment.

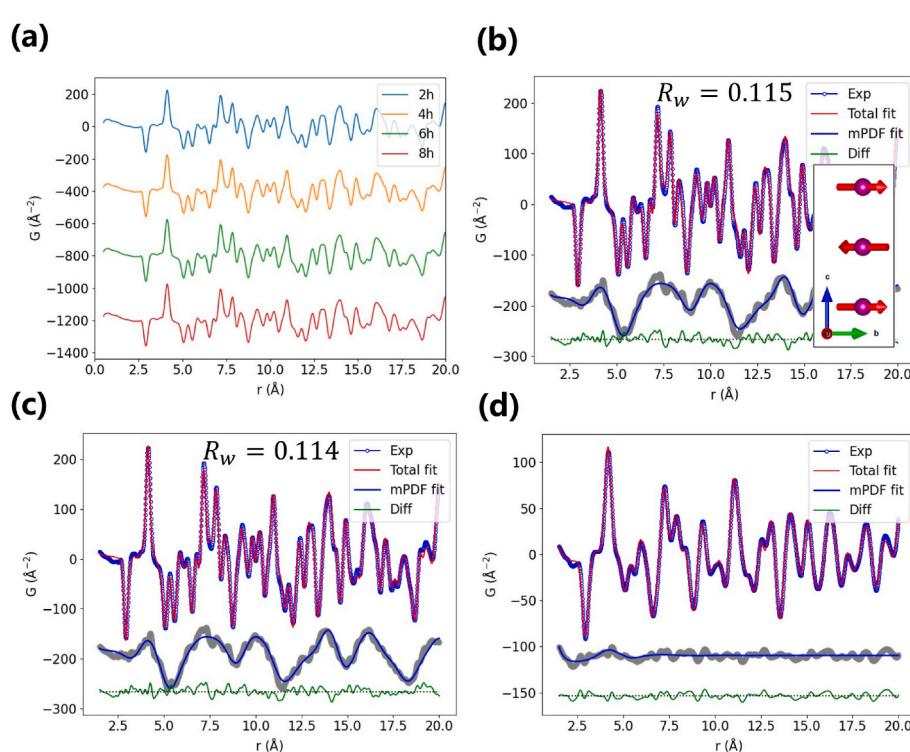The neutron total scattering experiment for mPDF analysis would be

Fig. 4. (a) The experimental PDF of MnTe at 20 K collected in different exposure time. (b) and (c): The mPDF fits for MnTe data at 20 K (b) collected in 2 h and (c) 8 h. (d) The mPDF fits for MnTe data at 400 K.

promising in unveiling the intricate secrets of complex magnetic systems. Taking the non-colinear kagome magnetic structures in quantum spin liquids as an example, these structures pose significant challenges for conventional diffraction characterizations. However, the mPDF method can assist in directly revealing the complicated magnetic configurations in real space. The simulated mPDF pattern for a Mn^{2+} kagome lattice is displayed in Fig. S6, which is calculated using the same instrument resolution parameters of MPI. The geometrically frustrated magnetic structure can be well described by the short-range real-space magnetic correlations. Noteworthily, analogous to atomic PDF, mPDF is suitable for characterizing materials without long-range magnetic ordering. Therefore, MPI is promising for characterizing complicated magnetic alignments such as spin glasses and spin liquids in real space in the future.

4. Conclusion

The magnetic pair distribution function (mPDF) method offers valuable insights into short-range magnetic correlations at the sub-nanometer length scale in real space, which is complementary to the average structure information obtained through conventional neutron diffraction. We carried out experiments to characterize the short-range local magnetic structure at the MPI instrument at CSNS, which is one of the newest neutron time-of-flight total scattering diffractometers. We measured the antiferromagnetic MnO and the altermagnetic candidate MnTe samples, providing a systematic benchmark for experiment and data processing parameters required for mPDF data collection, including exposure time, Q_{max}, and data smooth modifications. Through detailed local structure refinements, we confirmed the feasibility of collecting high-quality mPDF data at the MPI. In the future, it would be highly motivated to expand the application of the mPDF methodology to study more challenging magnetic systems, providing unique local magnetic structure information in the frontiers of condensed matter physics.

CRediT authorship contribution statement

Long Yang: Writing – review & editing, Writing – original draft, Visualization, Supervision, Software, Project administration, Methodology, Funding acquisition, Formal analysis, Data curation, Conceptualization. **Te Kang:** Writing – review & editing, Validation, Software, Investigation, Formal analysis, Data curation. **Juping Xu:** Writing – review & editing, Visualization, Software, Resources, Investigation, Formal analysis, Data curation. **Wen Yin:** Writing – review & editing, Resources, Investigation, Funding acquisition.

Declaration of competing interest

The authors declare that they have no known competing financial interests or personal relationships that could have appeared to influence the work reported in this paper.

Acknowledgements

Appendix A. Supplementary data

Supplementary data to this article can be found online at https://doi.org/10.1016/j.nima.2024.169967.

Data availability

Data will be made available on request.

References

[1] D.N. Basov, A.V. Chubukov, Manifesto for a higher Tc, Nat. Phys. 7 (2011) 272–276, https://doi.org/10.1038/nphys1975.

[2] E. Fradkin, S.A. Kivelson, J.M. Tranquada, Colloquium: theory of intertwined orders in high temperature superconductors, Rev. Mod. Phys. 87 (2015) 457–482, https://doi.org/10.1103/RevModPhys.87.457.

[3] E. Dagotto, T. Hotta, A. Moreo, Colossal magnetoresistant materials: the key role of phase separation, Phys. Rep. 344 (2001) 1–153, https://doi.org/10.1016/S0370-1573(00)00121-6.

[4] Y. Zhang, Y. Ni, H. Zhao, S. Hakani, F. Ye, L. DeLong, I. Kimchi, G. Cao, Control of chiral orbital currents in a colossal magnetoresistance material, Nature 611 (2022) 467–472, https://doi.org/10.1038/s41586-022-05262-3.

[5] Z. Qiu, D. Hou, J. Barker, K. Yamamoto, O. Gomonay, E. Saitoh, Spin colossal magnetoresistance in an antiferromagnetic insulator, Nat. Mater. 17 (2018) 577–580, https://doi.org/10.1038/s41563-018-0087-4.

[6] M. Fiebig, T. Lottermoser, D. Meier, M. Trassin, The evolution of multiferroics, Nat. Rev. Mater. 1 (2016) 1–14, https://doi.org/10.1038/natrevmats.2016.46.

[7] S. Dong, H. Xiang, E. Dagotto, Magnetoelectricity in multiferroics: a theoretical perspective, Natl. Sci. Rev. 6 (2019) 629–641, https://doi.org/10.1093/nsr/nwz023.

[8] C.G. Shull, W.A. Strauser, E.O. Wollan, Neutron diffraction by paramagnetic and antiferromagnetic substances, Phys. Rev. 83 (1951) 333–345, https://doi.org/10.1103/PhysRev.83.333.

[9] C.G. Shull, J.S. Smart, Detection of antiferromagnetism by neutron diffraction, Phys. Rev. 76 (1949) 1256–1257, https://doi.org/10.1103/PhysRev.76.1256.2.

[10] C.G. Shull, E.O. Wollan, W.C. Koehler, Neutron scattering and polarization by ferromagnetic materials, Phys. Rev. 84 (1951) 912–921, https://doi.org/10.1103/PhysRev.84.912.

[11] K.M. Nuttall, C.Z. Suggs, H.E. Fischer, M.M. Bordelon, S.D. Wilson, B.A. Frandsen, Quantitative investigation of the short-range magnetic correlations in the candidate quantum spin liquid $NaYbO_2$, Phys. Rev. B 108 (2023) L140411, https://doi.org/10.1103/PhysRevB.108.L140411.

[12] C. Broholm, R.J. Cava, S.A. Kivelson, D.G. Nocera, M.R. Norman, T. Senthil, Quantum spin liquids, Science 367 (2020) eaay0668, https://doi.org/10.1126/science.aay0668.

[13] Y. Zhang, T. Scholz, R. Dronskowski, M.T. McDonnell, M.G. Tucker, Local magnetic cluster size identified by neutron total scattering in the site-diluted spin glass $Sn_xFe_{4-x}N$ (x = 0.88), Phys. Rev. B 100 (2019) 014419, https://doi.org/10.1103/PhysRevB.100.014419.

[14] K. Binder, A.P. Young, Spin glasses: experimental facts, theoretical concepts, and open questions, Rev. Mod. Phys. 58 (1986) 801–976, https://doi.org/10.1103/RevModPhys.58.801.

[15] J.K. Furdyna, Diluted magnetic semiconductors, J. Appl. Phys. 64 (1988) R29–R64, https://doi.org/10.1063/1.341700.

[16] T. Dietl, A ten-year perspective on dilute magnetic semiconductors and oxides, Nat. Mater. 9 (2010) 965–974, https://doi.org/10.1038/nmat2898.

[17] T. Egami, S.J.L. Billinge, Underneath the Bragg Peaks: Structural Analysis of Complex Materials, second ed., Elsevier, Amsterdam, 2012.

[18] C.A. Young, A.L. Goodwin, Applications of pair distribution function methods to contemporary problems in materials chemistry, J. Mater. Chem. 21 (2011) 6464–6476, https://doi.org/10.1039/C0JM04415F.

[19] D.A. Keen, A.L. Goodwin, The crystallography of correlated disorder, Nature 521 (2015) 303–309, https://doi.org/10.1038/nature14453.

[20] S.J.L. Billinge, S.H. Skjærvø, M.W. Terban, S. Tao, L. Yang, Y. Rakita, B. A. Frandsen, Local structure determination using total scattering data, in: Reference Module in Chemistry, Molecular Sciences and Chemical Engineering, Elsevier, Oxford, 2023, https://doi.org/10.1016/B978-0-12-823144-9.00040-6.

[21] B. Frandsen, X. Yang, S.J.L. Billinge, Magnetic pair distribution function analysis of local magnetic correlations, Acta Cryst. A 70 (2014) 3–11, https://doi.org/10.1107/S2053273313033081.

[22] B.A. Frandsen, M. Brunelli, K. Page, Y.J. Uemura, J.B. Staunton, S.J.L. Billinge, Verification of anderson superexchange in MnO via magnetic pair distribution function analysis and *ab initio* theory, Phys. Rev. Lett. 116 (2016) 197204, https://doi.org/10.1103/PhysRevLett.116.197204.

[23] B.A. Frandsen, R. Baral, B. Winn, V.O. Garlea, Magnetic pair distribution function data using polarized neutrons and *ad hoc* corrections, J. Appl. Phys. 132 (2022) 223909, https://doi.org/10.1063/5.0130400.

[24] J.A.M. Paddison, M.J. Gutmann, J.R. Stewart, M.G. Tucker, M.T. Dove, D.A. Keen, A.L. Goodwin, Magnetic structure of paramagnetic MnO, Phys. Rev. B 97 (2018) 014429, https://doi.org/10.1103/PhysRevB.97.014429.

[25] T. Proffen, T. Egami, S.J.L. Billinge, A.K. Cheetham, D. Louca, J.B. Parise, Building a high resolution total scattering powder diffractometer – upgrade of NPD at MLNSC, Appl. Phys. A 74 (2002) s163–s165, https://doi.org/10.1007/s003390201929.

[26] J. Neuefeind, M. Feygenson, J. Carruth, R. Hoffmann, K.K. Chipley, The nanoscale ordered MAterials diffractometer NOMAD at the spallation neutron source SNS, Nucl. Instrum. Methods Phys. Res. B 287 (2012) 68–75, https://doi.org/10.1016/j.nimb.2012.05.037.

[27] K. Kodama, K. Ikeda, S. Shamoto, T. Otomo, Alternative equation on magnetic pair distribution function for quantitative analysis, J. Phys. Soc. Jpn. 86 (2017) 124708, https://doi.org/10.7566/JPSJ.86.124708.

[28] E. Lefrançois, L. Mangin-Thro, E. Lhotel, J. Robert, S. Petit, V. Cathelin, H. E. Fischer, C.V. Colin, F. Damay, J. Ollivier, P. Lejay, L.C. Chapon, V. Simonet, R. Ballou, Spin decoupling under a staggered field in the $Gd_2Ir_2O_7$ pyrochlore, Phys. Rev. B 99 (2019) 060401, https://doi.org/10.1103/PhysRevB.99.060401.

[29] R. Baral, A.V. Haglund, J. Liu, A.I. Kolesnikov, D. Mandrus, S. Calder, Local spin structure in the layered van der Waals materials $MnPS_xSe_{3-x}$, Phys. Rev. B 110 (2024) 014423, https://doi.org/10.1103/PhysRevB.110.014423.

[30] J. Xu, Y. Xia, Z. Li, H. Chen, X. Wang, Z. Sun, W. Yin, Multi-physics instrument: total scattering neutron time-of-flight diffractometer at China Spallation Neutron Source, Nucl. Instrum. Methods Phys. Res. 1013 (2021) 165642, https://doi.org/10.1016/j.nima.2021.165642.

[31] W.L. Roth, Magnetic structures of MnO, FeO, CoO, and NiO, Phys. Rev. 110 (1958) 1333–1341, https://doi.org/10.1103/PhysRev.110.1333.

[32] B.A. Frandsen, S.J.L. Billinge, Magnetic structure determination from the magnetic pair distribution function (mPDF): ground state of MnO, Acta Cryst. A 71 (2015) 325–334, https://doi.org/10.1107/S205327331500306X.

[33] B.A. Frandsen, P.K. Hamilton, J.A. Christensen, E. Stubben, S.J.L. Billinge, Diffpy. mpdf: Open-source software for magnetic pair distribution function analysis, J. Appl. Cryst. 55 (2022) 1377–1382, https://doi.org/10.1107/S1600576722007257.

[34] I.I. Mazin, Altermagnetism in MnTe: origin, predicted manifestations, and routes to detwinning, Phys. Rev. B 107 (2023) L100418, https://doi.org/10.1103/PhysRevB.107.L100418.

[35] M.M.H. Polash, F. Mohaddes, M. Rasoulianboroujeni, D. Vashaee, Magnon-drag thermopower in antiferromagnets *versus* ferromagnets, J. Mater. Chem. C 8 (2020) 4049–4057, https://doi.org/10.1039/C9TC06330G.

[36] Y. Zheng, T. Lu, M.M.H. Polash, M. Rasoulianboroujeni, N. Liu, M.E. Manley, Y. Deng, P.J. Sun, X.L. Chen, R.P. Hermann, D. Vashaee, J.P. Heremans, H. Zhao, Paramagnon drag in high thermoelectric figure of merit Li-doped MnTe, Sci. Adv. 5 (2019) eaat9461, https://doi.org/10.1126/sciadv.aat9461.

[37] R. Baral, J. Christensen, P. Hamilton, F. Ye, K. Chesnel, T.D. Sparks, R. Ward, J. Yan, M.A. McGuire, M.E. Manley, J.B. Staunton, R.P. Hermann, B.A. Frandsen, Real-space visualization of short-range antiferromagnetic correlations in a magnetically enhanced thermoelectric, Matter 5 (2022) 1853–1864, https://doi.org/10.1016/j.matt.2022.03.011.

[38] N. Roth, A.F. May, F. Ye, B.C. Chakoumakos, B.B. Iversen, Model-free reconstruction of magnetic correlations in frustrated magnets, IUCrJ 5 (2018) 410–416, https://doi.org/10.1107/S2052252518006590.

[39] Y. Xu, W. Li, C. Wang, J. Li, Z. Chen, S. Lin, Y. Chen, Y. Pei, Performance optimization and single parabolic band behavior of thermoelectric MnTe, J. Mater. Chem. A 5 (2017) 19143–19150, https://doi.org/10.1039/C7TA04842D.

[40] O. Arnold, J.C. Bilheux, J.M. Borreguero, A. Buts, S.I. Campbell, L. Chapon, M. Doucet, N. Draper, R. Ferraz Leal, M.A. Gigg, V.E. Lynch, A. Markvardsen, D. J. Mikkelson, R.L. Mikkelson, R. Miller, K. Palmen, P. Parker, G. Passos, T. G. Perring, P.F. Peterson, S. Ren, M.A. Reuter, A.T. Savici, J.W. Taylor, R.J. Taylor, R. Tolchenov, W. Zhou, J. Zikovsky, Mantid—data analysis and visualization package for neutron scattering and μ SR experiments, Nucl. Instrum. Methods Phys. Res. 764 (2014) 156–166, https://doi.org/10.1016/j.nima.2014.07.029.

[41] E. Lorch, Neutron diffraction by germania, silica and radiation-damaged silica glasses, J. Phys. C Solid State Phys. 2 (1969) 229–237, https://doi.org/10.1088/0022-3719/2/2/305.

[42] P. Juhás, C. Farrow, X. Yang, K. Knox, S.J.L. Billinge, Complex modeling: a strategy and software program for combining multiple information sources to solve ill posed structure and nanostructure inverse problems, Acta Cryst. A 71 (2015) 562–568, https://doi.org/10.1107/S2053273315014473.

[43] I.A. Blech, B.L. Averbach, Spin correlations in MnO, Physics Physique Fizika 1 (1964) 31–44, https://doi.org/10.1103/PhysicsPhysiqueFizika.1.31.

[44] A.L. Goodwin, M.G. Tucker, M.T. Dove, D.A. Keen, Magnetic structure of MnO at 10 K from total neutron scattering data, Phys. Rev. Lett. 96 (2006) 047209, https://doi.org/10.1103/PhysRevLett.96.047209.

[45] N. Kunitomi, Y. Hamaguchi, S. Anzai, Neutron diffraction study on manganese telluride, J. Phys. France 25 (1964) 568–574, https://doi.org/10.1051/jphys:01964002505056800.

[46] I.-K. Jeong, T. Proffen, F. Mohiuddin-Jacobs, S.J.L. Billinge, Measuring correlated atomic motion using X-ray diffraction, J. Phys. Chem. A 103 (1999) 921–924, https://doi.org/10.1021/jp9836978.

[47] D.W. Marquardt, An algorithm for least-squares estimation of nonlinear parameters, J. Soc. Indust. Appl. Math. 11 (1963) 431–441, https://doi.org/10.1137/0111030.

[48] K. Levenberg, A method for the solution of certain non-linear problems in least squares, Quart. Appl. Math. 2 (1944) 164–168, https://doi.org/10.1090/qam/10666.

[49] E. Jones, T. Oliphant, P. Peterson, SciPy: open source scientific tools for Python. http://www.scipy.org/, 2001.

[50] B.H. Toby, R.B. Von Dreele, GSAS-II: the genesis of a modern open-source all purpose crystallography software package, J. Appl. Cryst. 46 (2013) 544–549, https://doi.org/10.1107/S0021889813003531.

[51] S.V. Gallego, J.M. Perez-Mato, L. Elcoro, E.S. Tasci, R.M. Hanson, K. Momma, M. I. Aroyo, G. Madariaga, MAGNDATA: towards a database of magnetic structures. I. The commensurate case, J. Appl. Cryst. 49 (2016) 1750–1776, https://doi.org/10.1107/S1600576716012863.

[52] J. Krempaský, L. Šmejkal, S.W. D'Souza, M. Hajlaoui, G. Springholz, K. Uhlířová, F. Alarab, P.C. Constantinou, V. Strocov, D. Usanov, W.R. Pudelko, R. González-Hernández, A. Birk Hellenes, Z. Jansa, H. Reichlová, Z. Šobáň, R.D. Gonzalez Betancourt, P. Wadley, J. Sinova, D. Kriegner, J. Minár, J.H. Dil, T. Jungwirth, Altermagnetic lifting of Kramers spin degeneracy, Nature 626 (2024) 517–522, https://doi.org/10.1038/s41586-023-06907-7.

[53] W. Szuszkiewicz, E. Dynowska, B. Witkowska, B. Hennion, Spin-wave measurements on hexagonal MnTe of NiAs-type structure by inelastic neutron scattering, Phys. Rev. B 73 (2006) 104403, https://doi.org/10.1103/PhysRevB.73.104403.